ChemComm



COMMUNICATION

View Article Online

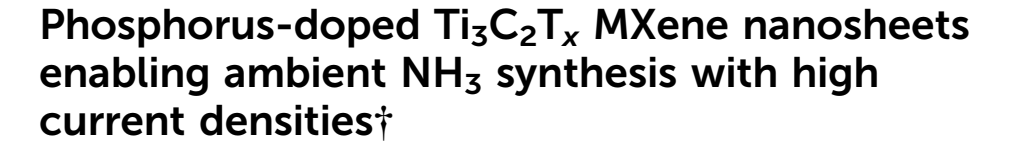


Cite this: Chem. Commun., 2024, 60, 8728

Received 23rd June 2024, Accepted 19th July 2024

DOI: 10.1039/d4cc03051f

rsc.li/chemcomm



Yuchuan Qi,‡a Xianghua Hou,‡a Ziying He,*b Fan He,a Tianran Wei,bc Ge Meng,*ab Huihui Hu,^c Qian Liu,^d Guangzhi Hu and Xijun Liu *c

Herein, we show that P-doped Ti₃C₂T_x MXene nanosheets can effectively catalyze the NO₃RR-to-NH₃ conversion with a high faradaic efficiency of 95% and a yield rate of 5.39 mg h⁻¹ mg_{cat} ⁻¹. Moreover, the catalyst achieves an impressive high current density of -1200 mA cm^{-2} at a low potential of -1.51 V, accompanied by an NH_3 productivity of 123.5 mg h^{-1} mg_{cat.} $^{-1}$. Theoretical calculations further reveal that phosphorous dopants facilitate the adsorption and activation of reactants/intermediates and thus lower the energy barrier.

NH₃ assumes a significant role in the nitrogen cycle and represents a pivotal compound in fertilizers, explosives, plastics, and so on. 1-3 Generally, its industrial production strongly relies on the Haber-Bosch approach, 4,5 leading to great energy consumption and greenhouse gas emissions. In this case, NH₃ synthesized by the N2 reduction reaction (NRR) under ambient conditions has gained much attention in recent years.^{6,7} However, the poor solubility and inert chemical reactivity of N2 molecules typically contribute to unsatisfactory selectivity and NH3 yield rates. Therefore, the development of more efficient electrocatalytic systems is highly desirable.

More recently, the nitrate reduction reaction (NO₃RR) demonstrates advancement as compared to the NRR because of its low N=O cracking energy and good solubility, 8,9 therefore

E-mail: 2021028852@gxgy.edu.cn, mengge@wzu.edu.cn

endowing NH₃ synthesis with a fast reaction rate. Besides, the NO₃RR can also alleviate the ever-increasing NO₃⁻ pollution in water. 10-12 In this regard, the NO₃RR acts as a dual-purpose strategy. To date, considerable efforts have been devoted to designing high-performance NO₃RR catalysts, such as RuO_x, ¹³ CuO_r, ¹⁴ CoO_r, ¹⁵ and single-atom materials. ¹⁶ However, these catalysts typically deliver small current densities (<100 mA cm⁻²), indicative of low yield rates. That is, the industrial application of the NO₃RR cannot be technically achieved. Hence, the NO₃RR-to-NH₃ conversion under large current densities is still a longstanding and challenging task.

The Ti₃C₂T_x MXene is exactly considered a promising catalyst for various electrochemical reactions due to its large exposure area, high conductivity, and tunable surface chemistry. 17-19 Current reports have proved that Ti₃C₂T_x-based catalysts can efficiently catalyze nitrate reduction to yield NH3 with high faradaic efficiencies (FEs > 80%). 20-22 However, the obtained current densities are limited, and further improvement is needed. In this context, we introduced a phosphorus element into the Ti₃C₂T_x MXene (namely P-Ti₃C₂T_x) to realize high-performance NO₃RR-to-NH₃ conversion, which showed a maximal FE of 95% and a corresponding yield rate of 5.39 mg h⁻¹ mg_{cat}⁻¹ at a potential of -1.2 V versus reversible hydrogen electrode (vs. RHE). Besides, the catalyst exhibited a stable activity over 6 cycles and 40-h long-term electrolysis. Impressively, when examined in a flow cell, the catalyst delivered a notable high current density of -1200 mA cm⁻² at a low potential of -1.51 V vs. RHE, accompanied by a yield rate of 123.5 mg h⁻¹ mg_{cat.}⁻¹, implying the potential application for NH₃ synthesis. Moreover, in-depth simulations revealed that the phosphorus dopants can dramatically optimize the reactivity of Ti sites and reduce the energy barrier, accounting for excellent NO₃RR performance.

The synthetic procedure is illustrated in Fig. 1a, where the Ti₃AlC₂ raw materials were first etched using a mixture of LiF and HCl, and then the residue was further annealed in the presence of NaH₂PO₂ to generate P-Ti₃C₂T_r. The representative scanning electron microscopy (SEM) images of Ti₃C₂T_x and

^a Key Laboratory of Carbon Materials of Zhejiang Province, College of Chemistry and Materials Engineering, Wenzhou University, Wenzhou 325035, China.

^b Guangxi Vocational & Technical Institute of Industry, Nanning 530001, Guangxi,

^c MOE Key Laboratory of New Processing Technology for Nonferrous Metals and Materials, School of Resources, Environment and Materials, Guangxi University, Nanning, 530004 Guangxi, China. E-mail: xjliu@gxu.edu.cn

^d Institute for Advanced Study, Chengdu University, Chengdu 610106, Sichuan,

^e School of Ecology and Environmental Science, Yunnan University, Kunming 650504, China

[†] Electronic supplementary information (ESI) available. See DOI: https://doi.org/ 10.1039/d4cc03051f

[‡] These authors contributed equally to this work.

Communication ChemComm

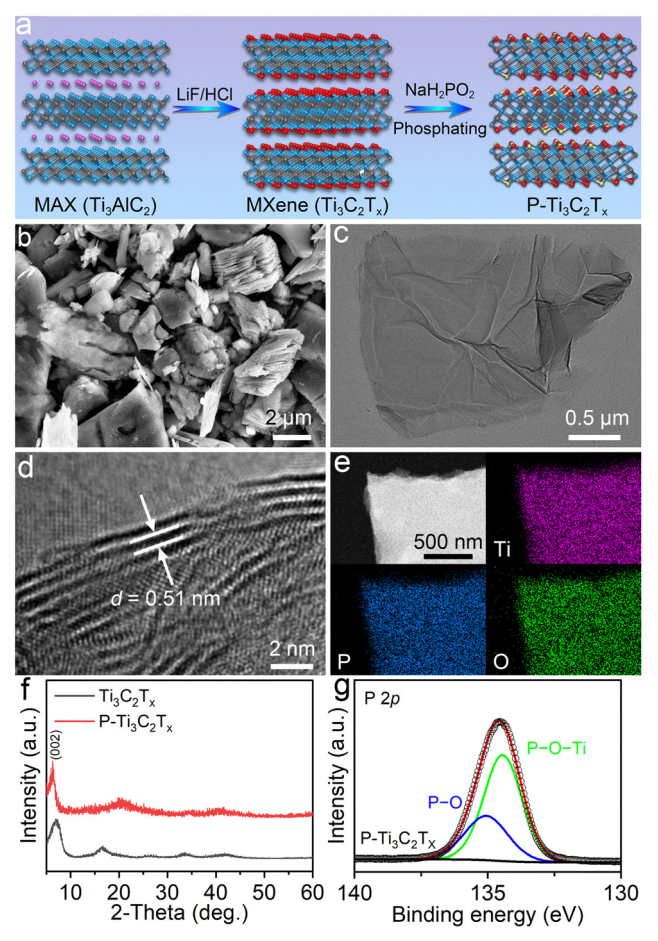


Fig. 1 (a) Schematic of the synthesis of $P-Ti_3C_2T_x$. (b)-(d) SEM, TEM and HRTEM images. (e) EDX elemental mapping images. (f) XRD patterns. (g) High-resolution P 2p XPS spectrum.

P-Ti₃C₂T_r are shown in Fig. S1 (ESI[†]) and Fig. 1b, respectively, which clearly present sheet-like morphology, indicative of a large surface area. This favors the exposure of active sites and mass transfer during the electrolysis. The transmission electron microscopy (TEM) image in Fig. 1c confirms the multilayer lamellar structure. The high-resolution TEM (HRTEM) image reveals atomic crystal fringes with a size of 0.51 nm corresponding to the (002) plane of Ti₃C₂T_x (Fig. 1d). Meanwhile, the energy-dispersive X-ray (EDX) images in Fig. 1e manifest the uniform distribution of Ti, P, and O on the surface of the nanosheet.

Further, the X-ray diffraction (XRD) patterns were collected and are displayed in Fig. 1f, which show characteristic peaks of the typical Ti₃C₂T_x MXene, in line with previous reports. Compared to pristine Ti₃C₂T_x, the (002) peak of P-Ti₃C₂T_x slightly shifts to a small angle, suggesting an increased lattice spacing.²³ Moreover, applying X-ray photoelectron spectroscopy (XPS) measurements, the survey spectrum in Fig. S2 (ESI†) also revealed the presence of the P element in P-Ti₃C₂T_x, conforming to the results of EDX (Fig. 1e). The high-resolution P 2p spectrum (Fig. 1g) could be deconvoluted into two peaks at 134.4 and 135.1 eV, corresponding to P-O-Ti and P-O bonds,

respectively.²⁴ Besides, as observed in the Ti 2p XPS spectrum of P-Ti₃C₂T_x, the peaks at 454.8, 455.7, 456.5, and 458.3 are ascribed to Ti-C, Ti2+, Ti3+, and Ti-O, respectively (Fig. S3, ESI†). 25 Additionally, the O 1s XPS spectrum was deconvoluted into three peaks (Fig. S4, ESI†), which are interpreted as those of Ti-O (531.7 eV), Ti-O_x (532.8 eV), and C-Ti-(OH)_x (534.0 eV). 26 The results further confirm the thriving synthesis of P-Ti₃C₂T_x. In addition, the optimal P content in P-Ti₃C₂T_r was determined to be 5.8 wt% according to the XPS results (Fig. S5, ESI†).

Next, the NO₃RR activity of the as-prepared samples was checked by using a three-electrode configuration in a neutral electrolyte (0.5 M K₂SO₄ + 0.1 M KNO₃). The optimal catalyst loading was found to be 0.15 mg cm⁻² (Fig. S6 and S7, ESI†). The linear scanning voltammetry (LSV) curves were first studied, and the results revealed that P-Ti₃C₂T_x delivers larger current densities as compared to Ti₃C₂T_x (Fig. 2a). This suggests a higher NO₃RR activity on P-Ti₃C₂T_x. In addition, the current densities of P-Ti₃C₂T_x obtained in the blank electrolyte are lower than those in NO₃-containing electrolyte (Fig. S8, ESI†), implying that P-Ti₃C₂T_x can effectively catalyze the reduction of NO₃^{-.27} The absorbance of the dilute electrolyte was measured by a reported indophenol blue method.^{28,29} As a result, FEs exhibited a volcanic trend in Fig. 2b and c due to the existence of a competitive hydrogen evolution reaction (HER),28 which achieves a maximal FE of 95% at -1.2 V vs. RHE, larger than that on $Ti_3C_2T_r$ (81% at -1.1 V vs. RHE). Meanwhile, it can be seen that the FEs for NH₃ production are above 80% over the wide potential range, which indicates that the HER is inactive. More importantly, the measured NH₃ yield rate of P-Ti₃C₂T_x

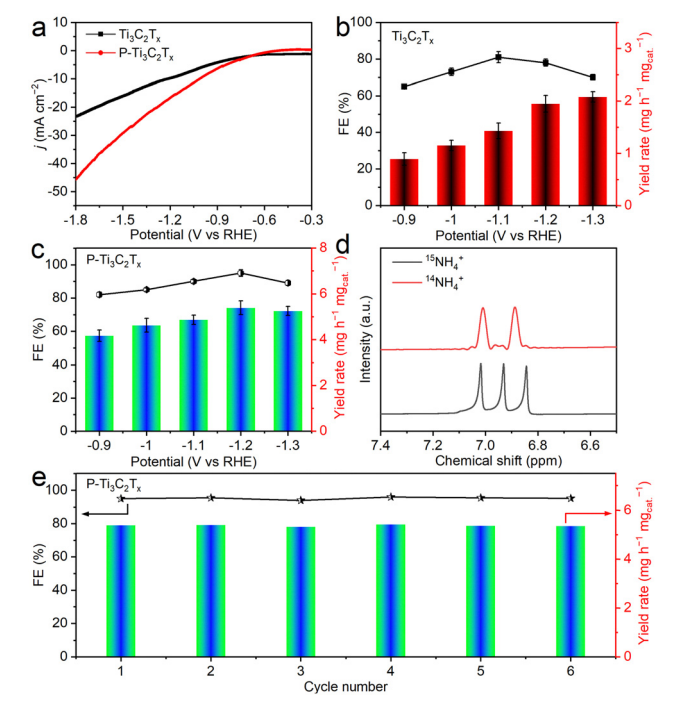


Fig. 2 (a) LSV curves in NO₃⁻-containing electrolytes in an H cell. (b) and (c) The obtained FEs and yield rates for $Ti_3C_2T_x$ and $P-Ti_3C_2T_x$. (d) The ¹H NMR spectrum. (e) Cycling stability

ChemComm Communication

reached 5.39 mg h⁻¹ mg_{cat.}⁻¹, significantly higher than that of pure Ti₃C₂T_x and most of the currently reported catalysts (Table S1, ESI†). When tested in a dilute electrolyte, P-Ti₃C₂T_x presents the highest FE of 90% at $-1.1 \text{ V} \nu s$. RHE (Fig. S9, ESI†).

Subsequently, the by-products of NO2-, N2H4, and H2 are displayed in Fig. S10-S12 (ESI†), which shows that the FEs for NO₂ and N₂H₄ are negligible, revealing the superior selectivity of NO₃RR-to-NH₃ on P-Ti₃C₂T_r. To verify the origin of produced NH₃, isotopic labeling tests were performed and the results are depicted in Fig. 2d, which show two characteristic peaks corresponding to ¹⁵NH₄⁺, implying that the source of nitrogen in the generated NH₃ is indeed from the reduction of NO₃⁻.³⁰ In addition, alternate electrolysis of the three-group cycles in electrolytes with and without NO₃ confirms that NH₃ is merely produced from the NO₃RR rather than other contaminants (Fig. S13, ESI \dagger). Fig. 2e shows multiple cycling tests at -1.2 Vvs. RHE and no clear decay in FEs and yield rates is observed, confirming the stable electrochemical activity of P-Ti₃C₂T_r. Besides, the current density presented little fluctuation during the 40-h electrolysis (Fig. S14, ESI†). Furthermore, XRD patterns and SEM and TEM images manifest the robustness of P-Ti₃C₂T_r (Fig. S15-S17, ESI†).

The results of double-layer capacitance demonstrated that P-Ti₃C₂T_x possesses a higher active surface area compared to $Ti_3C_2T_x$ (Fig. S18, ESI†), indicative of more exposed sites for the NO₃RR. Nyquist plots further confirmed an improved efficiency for ionic transport and a low resistance for charge transfer (Fig. S19, ESI†).

The large-scale NH₃ production is vital for the commercialization of the NO₃RR.^{8,31,32} In this case, we further examined the NO₃RR activity of P-Ti₃C₂T_x in a flow cell and the results are depicted in Fig. 3. Clearly, P-Ti₃C₂T_x drives the current densities to -1000 and -1500 mA cm⁻² at -1.30 and -1.51 V vs. RHE, respectively, obviously superior to that of pure Ti₃C₂T_x (Fig. 3a). The corresponding FEs at different current densities are depicted in Fig. 3b and reach the highest FE of 92% at a current density of -1000 mA cm⁻², and the yield rate achieves a maximum of

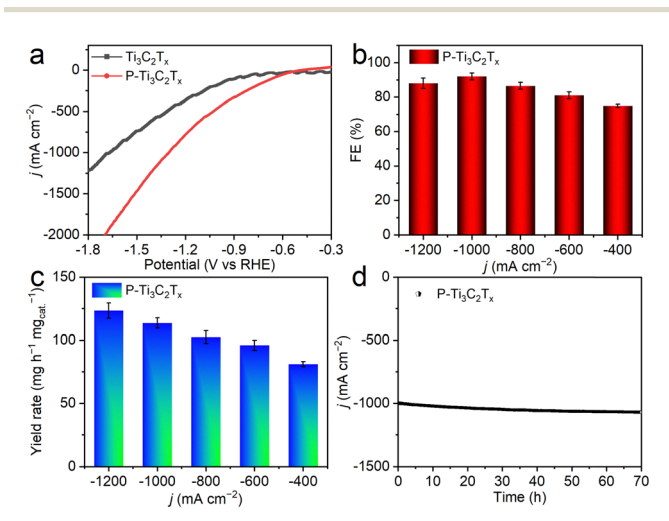


Fig. 3 (a) LSV curves in a flow cell. (b) and (c) FEs and yield rates at different current densities. (d) Stability test at -1000 mA cm⁻².

123.5 mg h^{-1} mg_{cat.}⁻¹ at -1200 mA cm⁻² (Fig. 3c), comparable to the best results (Table S2, ESI†). Besides, the obtained yield rate at the optimal potential in a flow cell is obviously larger than that in an H cell, while the FEs are comparable (Fig. S20, ESI†).

Next, the NO₃RR stability of P-Ti₃C₂T_x was assessed and the result showed that no notable discrepancy in FEs was observed after 70-h electrolysis (Fig. 3d), suggesting that P-Ti₃C₂T_x is chemically stable as a catalyst during the reduction process.

To gain an in-depth insight into the NO₃RR enhancement of phosphorus-doping, density functional theory (DFT) calculations were conducted. As depicted in Fig. 4a, the introduced phosphorus facilitates the adsorption of NO_3^- (ΔE_{ab}) with a large value of −1.61 eV as compared to a pure Ti₃C₂T_x surface (-1.53 eV), implying P-Ti₃C₂T_x offers a strong affinity to the reactant. 33-35 The phosphorus-doping also promoted the charge transfer between NO₃⁻ and the catalyst surface, and the Bader analyses indicated that a charge of 0.63 e is transferred from P-Ti₃C₂T_x to the adsorbed NO₃ $^-$ (Fig. 4b). Based on these, NO₃ $^$ can be adsorbed and activated energetically preferred on the P-Ti₃C₂T_r surface.³⁶

Then, the energy barrier for the competitive HER was considered and the results are shown in Fig. 4c. As expected, P-Ti₃C₂T_x had a higher H* free energy (0.14 eV) than Ti₃C₂T_x (0.02 eV), indicative of the inhibition of hydrogen generation during the NO₃RR process. Moreover, the DFT results show that the potential-determining step (PDS) on P-Ti₃C₂T_r corresponds to *NO₂ + H⁺ + e⁻ \rightarrow *NO₂H with an energy barrier of 1.02 eV (Fig. 4d), while after phosphorus-doping, this barrier could be greatly reduced to 0.41 eV, suggesting that dopants are responsible for the NO₃RR enhancement, 37 as revealed by the above experiments. It is also found that the subsequent elementary reactions follow a spontaneous exothermic process. Combined with experimental and theoretical analyses, we could infer that the excellent NO₃RR performance indeed originates from heteroatom doping.

In summary, P-Ti₃C₂T_x proved to be an advanced NO₃RR catalyst for NH3 synthesis under ambient conditions. In neutral media, the

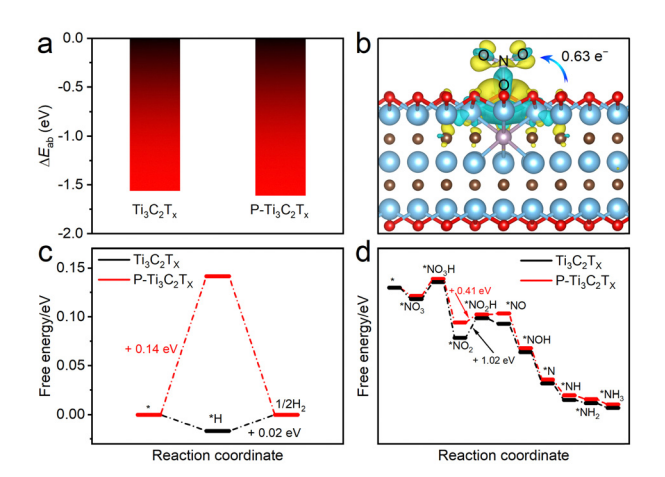


Fig. 4 (a) ΔE_{ab} of NO_3^- on the catalyst surface. (b) Charge density difference. Note that yellow and cyan shadows represent charge accumulation and depletion in the space, respectively. (c) and (d) Calculated free energy profiles for the HER and NO₃RR

Communication ChemComm

catalyst achieved a high yield rate of 5.39 mg h⁻¹ mg_{cat.}⁻¹ and a maximal FE of 95% with good cycling stability. More impressively, when tested in a flow cell, the catalyst delivers an amperelevel current density at a low working potential, accompanied by a high NH₃ FE, strongly suggesting the promising application in future large-scale NH₃ production. Based on the DFT studies, doping phosphorus atoms into Ti₃C₂T_x can offer abundant active sites and modulate the electronic structure, efficiently promoting the adsorption and activation of reactants and intermediates and thereby lowering the NO₃RR energy barrier. In our work, an efficient catalyst is developed for the NO₃RR-to-NH₃ conversion at high current densities, which may be helpful for massive NH₃ production.

This work was financially supported by the National Natural Science Foundation of China (22109118 and 22075211).

Data availability

Data are available on request from the authors.

Conflicts of interest

There are no conflicts to declare.

Notes and references

- 1 N. Gruber and J. N. Galloway, Nature, 2008, 451, 293.
- 2 M. Yang, T. Wei, J. He, Q. Liu, L. Feng, H. Li, J. Luo and X. Liu, Nano Res., 2024, 17, 1209.
- 3 M. Fu, Y. Mao, H. Wang, W. Luo, Y. Jiang, W. Shen, M. Li and R. He, Chin. Chem. Lett., 2024, 35, 108341.
- 4 L. Zhang, X.-Y. Xie, H. Wang, L. Ji, Y. Zhang, H. Chen, T. Li, Y. Luo, G. Cui and X. Sun, Chem. Commun., 2019, 55, 4627-4630.
- 5 X. Zou, J. Xie, C. Wang, G. Jiang, K. Tang and C. Chen, Chin. Chem. Lett., 2023, 34, 107908.
- 6 L. Lv, H. Tan, Y. Kong, B. Tang, Q. Ji, Y. Liu, C. Wang, Z. Zhuang, H. Wang, M. Ge, M. Fan, D. Wang and W. Yan, Angew. Chem., Int. Ed., 2024, 63, e202401943.
- 7 W. Qiu, S. Qin, Y. Li, N. Cao, W. Cui, Z. Zhang, Z. Zhuang, D. Wang and Y. Zhang, Angew. Chem., Int. Ed., 2024, 63, e202402684.
- 8 G. Zhang, G. Wang, Y. Wan, X. Liu and K. Chu, ACS Nano, 2023,
- 9 K. Chen, Z. Ma, X. Li, J. Kang, D. Ma and K. Chu, Adv. Funct. Mater., 2023, 33, 2209890.
- 10 J. Liang, Q. Liu, A. A. Alshehri and X. Sun, Nano Res. Energy, 2022, 1, 9120010.
- 11 H. Yang, X. Jiang, J. Sun, B. Zhang, X. Su, Q. Wu, Z. Qu and S. Huo, J. Alloys Compd., 2024, 989, 174402.

- 12 H. Yang, B. Zhang, J. Sun, X. Su, S. Huo and Z. Qu, J. Alloys Compd., 2024, 997, 174956.
- 13 J. Li, G. Zhan, J. Yang, F. Quan, C. Mao, Y. Liu, B. Wang, F. Lei, L. Li, A. W. M. Chan, L. Xu, Y. Shi, Y. Du, W. Hao, P. K. Wong, J. Wang, S.-X. Dou, L. Zhang and J. C. Yu, J. Am. Chem. Soc., 2020, 142,
- 14 S. Chen, G. Qi, R. Yin, Q. Liu, L. Feng, X. Feng, G. Hu, J. Luo, X. Liu and W. Liu, Nanoscale, 2023, 15, 19577.
- 15 N. Sun, Y. Guo, L. Luo, X. Cai, S. Shen and J. Zhang, Appl. Surf. Sci., 2023, 624, 157118.
- 16 W. Zhang, X. Qin, T. Wei, Q. Liu, J. Luo and X. Liu, J. Colloid Interface Sci., 2023, 638, 650-657.
- 17 P. Liu, P. Xiao, M. Lu, H. Wang, N. Jin and Z. Lin, Chin. Chem. Lett., 2023, 34, 107426.
- 18 J. Yang, F. Zhang and J. Chen, China Powder Sci. Technol., 2024, 30, 161.
- 19 J. Y. Loh, F. M. Yap and W.-J. Ong, J. Mater. Sci. Technol., 2024, **179.** 86.
- 20 M. Wang, T. Hu, C. Wang, F. Du, H. Yang, W. Sun, C. Guo and C. M. Li, Sci. China Mater., 2023, 66, 2750.
- 21 J. Theerthagiri, J. Park, H. T. Das, N. Rahamathulla, E. S. F. Cardoso, A. P. Murthy, G. Maia, D. V. N. Vo and M. Y. Choi, Environ. Chem. Lett., 2022, 20, 2929.
- 22 X. Yang, G. Wei, J. Cao, Z. Ding, R. Yuan, J. Long and C. Xu, ACS Sustainable Chem. Eng., 2024, 12, 3378-3389.
- 23 Y. Ren, F. Tian, L. Jin, Y. Wang, J. Yang, S. You and Y. Liu, Environ. Sci. Technol., 2023, 57, 10458.
- 24 M. Chao, K. Zeng, C. Lu, Z. Shi, J. Guo, X. Chen and R. Yang, J. Colloid Interface Sci., 2024, 657, 46.
- 25 X. Liu, M. Chen, J. Ma, J. Liang, C. Li, C. Chen and H. He, China Powder Sci. Technol., 2024, 30, 35.
- 26 C. Kaplan, R. M. Restrepo, T. Schultz, K. Li, V. Nicolosi, N. Koch and M. P. Browne, Electrochim. Acta, 2024, 490, 144269.
- 27 X. Hu, D. Zhou, H. Wang, W. Zhang, H. Zhong and Y. Chen, Chin. Chem. Lett., 2023, 34, 108050.
- 28 T. Hou, J. Ding, H. Zhang, S. Chen, Q. Liu, J. Luo and X. Liu, Mater. Chem. Front., 2023, 7, 4952.
- 29 X. Gao and E. C. M. Tse, Small, 2024, 20, 2306311.
- 30 G. E. Dima, A. C. A. de Vooys and M. T. M. Koper, J. Electroanal. Chem., 2003, 554-555, 15.
- 31 Y. Zhao, J. Zhang, X. Guo, X. Cao, S. Wang, H. Liu and G. Wang, Chem. Soc. Rev., 2023, 52, 3215.
- 32 Y. Ji, Z. Yu, L. Yan and W. Song, China Powder Sci. Technol., 2023, 29, 100.
- 33 K. Chen, J. Xiang, Y. Guo, X. Liu, X. Li and K. Chu, Nano Lett., 2024, 24, 541.
- 34 M. Ghosh, M. Ibrar and J. M. Smith, Chem. Commun., 2022, 58,
- 35 C. Zhang, H. Xu, Y. Wang, M. An, Y. Wang, Z. Yuan, W. Zhang, C. Li, M. Guo and D. Su, China Powder Sci. Technol., 2023,
- 36 O. Q. Carvalho, R. Marks, H. K. K. Nguyen, M. E. Vitale-Sullivan, S. C. Martinez, L. Árnadóttir and K. A. Stoerzinger, J. Am. Chem. Soc., 2022, 144, 14809.
- 37 J. Li, S. Yan, G. Li, Y. Wang, H. Xu and G. Duan, China Powder Sci. Technol., 2023, 29, 101.